Continuity Risk of Feature Extraction for Laser-Based Navigation

Mathieu Joerger
The University of Arizona, Tucson, Arizona, U.S.A., joerger@email.arizona.edu

Boris Pervan
Illinois Institute of Technology, Chicago, Illinois, U.S.A

BIOGRAPHIES

Dr. Mathieu Joerger is an assistant professor at the University of Arizona, working on multi-sensor integration, on sequential fault-detection for multi-constellation navigation systems, and on safety of sense and avoid for unmanned aircraft systems. Dr. Joerger obtained a Master in Mechatronics from the National Institute of Applied Sciences in Strasbourg, France, in 2002, and a M.S. and a Ph.D. in Mechanical and Aerospace Engineering from the Illinois Institute of Technology (IIT), in 2002 and 2009 respectively. He is the 2009 recipient of the Institute of Navigation (ION) Bradford Parkinson award, and the 2014 recipient of the ION Early Achievement Award.

Dr. Boris Pervan is a Professor of Mechanical and Aerospace Engineering at IIT. Prof. Pervan received his B.S. from the University of Notre Dame, M.S. from the California Institute of Technology, and Ph.D. from Stanford University. He is an Associate Fellow of the AIAA, a Fellow of the Institute of Navigation (ION), and Editor-in-Chief of the ION journal NAVIGATION. He was the recipient of the IIT Sigma Xi Excellence in University Research Award (2011, 2002), Ralph Barnett Mechanical and Aerospace Dept. Outstanding Teaching Award (2009, 2002), Mechanical and Aerospace Dept. Excellence in Research Award (2007), University Excellence in Teaching Award (2005), IEEE Aerospace and Electronic Systems Society M. Barry Carlton Award (1999), RTCA William E. Jackson Award (1996), Guggenheim Fellowship (Caltech 1987), and Albert J. Zahm Prize in Aeronautics (Notre Dame 1986).

ABSTRACT

In this paper, a new continuity risk evaluation method is developed, simulated, and tested for laser-based navigation algorithms using feature extraction (FE) and data association (DA). A major risk for safety in FE and DA is caused by incorrect association, which happens when attributing a feature extracted from laser data to the wrong landmark in a pre-established map. In prior work, we designed an innovation-based DA process to evaluate the integrity risk caused by incorrect associations while considering all potential measurement permutations. In this paper, permutations are used again at the FE step to determine the minimum normalized separation between extracted features. Features that are poorly separated are easily found, but are likely to be incorrectly associated. If the minimum separation is smaller than expected, then features are not extracted, which causes loss of navigation continuity. This paper provides an analytical upper-bound on the continuity risk caused by nominal laser measurement errors, and an integrity risk bound guaranteeing a predefined level of continuity. These safety risk bounds are analyzed and tested in example scenarios showing that the lower the continuity risk requirement is, the higher the integrity risk due to incorrect associations becomes.

INTRODUCTION

This paper describes the design, analysis and testing of a new integrity and continuity risk monitoring method for laser-based localization using feature extraction (FE) and data association (DA). FE and DA are pre-estimator data processing functions that are implemented in laser-based navigation applications [1-14]. This research builds upon prior work in [15] where an integrity risk prediction method for FE and DA was first established. The focus in this current paper is on continuity risk evaluation, and on quantifying the impact on navigation integrity of meeting a pre-defined continuity requirement. This work intends to *quantify risks* involved with FE and DA, thereby ensuring safety of laser-based localization for autonomous passenger vehicles (APV).

Currently, the most publicized efforts to demonstrate APV safety are Google's and Tesla's approaches to have APVs drive millions of miles with minimal human intervention. At this time, Google cars have autonomously travelled an impressive two million miles in urban areas [16]. Tesla's autopilot is reported to have driven more than 130 million miles –on highways only– before it caused a fatality in May 2016. In parallel, the National Highway Traffic Safety Administration (NHTSA) reports about one fatality in traffic accidents per 100 million mile driven by human drivers [17, 18]. But, this number accounts for incidents on all roads, in all weather conditions, and for all vehicle ages and types. Thus, a purely experimental, complete proof that APVs match the level of safety of human driving would require billions of miles driven. This is assuming that no fatalities occur during that time, that no major APV upgrade is performed, and that the testing environment is representative of all U.S. roads. Clearly, other methods must also be employed to ensure APV safety.

As a complement to testing, this research leverages prior analytical work carried out in civilian aviation navigation where safety is assessed in terms of integrity and continuity. These top-level quantifiable performance metrics are sensor- and platform-independent, and can thus be used to set certifiable requirements on individual system components to achieve and prove an overall level of safety. Integrity is a measure of trust in sensor information: integrity risk is the probability of undetected sensor errors causing unacceptably large positioning uncertainty [19]. Continuity is a measure of the navigation system's ability to operate without unscheduled interruption [19]. Both loss of integrity and loss of continuity can place the APV in hazardous situations.

Several methods have been established to predict the integrity and continuity risks in Global Navigation Satellite Systems (GNSS)-based aviation applications, which are instrumental in ensuring the safety of pilots and crew [19-22]. Unfortunately, the same methods do not apply to APVs, because ground vehicles operate under sky-obstructed areas where GNSS signals can be altered or even blocked by buildings and trees.

APVs require sensors in addition to GNSS, including laser scanners or radars, whose raw information must be pre-processed before it can be used for navigation [8, 23-24]. We focus on laser scanners because of their prevalence in APVs, of their market availability, and of our prior experience. A raw laser scan is made of thousands of data points, each of which individually does not carry any useful information. Raw laser data must be segmented or grouped to identify 'features', which are then processed for navigation.

Features in the perceived environment can include, for example, lines or planes corresponding to building walls in two- or three-dimensional scans, respectively. Features can be tracked over successive observations to provide relative 'pose' estimation (pose designates position and orientation). Previous knowledge of feature parameters, such as the coordinates in a local East-North-Up navigation frame of the vector normal to line- or plane-features, can be provided either by a landmark map, or by previous observations when using SLAM-type algorithms (SLAM stands for Simultaneous Localization And Mapping). Feature parameters can be used for APV pose estimation using an extended Kalman filter (EKF) [8,23,24].

To achieve this, two intermediary procedures must be carried out [2,5,7,8]. (1) 'Feature extraction' (FE) aims at identifying the few most consistently identifiable, distinguishable, and viewpoint-invariant landmarks in the raw laser scan. (2) 'Data association' (DA) assigns these extracted features to the corresponding mapped landmarks that are used in the EKF over successive observations. Incorrect association is a well-known problem that can lead to large navigation errors [25]. Several publications on multi-target tracking describe relevant approaches to evaluate the probability of correct association in the presence of measurement uncertainty [1, 26, 27]. However, these algorithms are not well suited for safety-critical APV applications due to their lack of prediction capability, to approximations that do not necessarily upper-bound risks, and to high computational loads. Overall, research on integrity and continuity of FE and DA is sparse.

In [15], we developed an analytical integrity risk prediction process for FE and DA. We established a multiple-hypothesis innovation-based DA method, which provides the means to evaluate the probability of incorrect associations while considering all potential measurement permutations. This algorithm was analyzed and tested to quantify the impact of incorrect associations on integrity risk, and the following key safety-tradeoff was pointed out: on the one hand, clearly distinguishable landmarks are desirable to avoid incorrect associations; but on the other hand, requiring large separation between features may prevent *continuous* navigation. How can we evaluate the continuity risk of FE and DA?

In response, in this work, we derive a new analytical method to rigorously quantify the continuity risk of laser-based navigation for applications to APV localization. The method guarantees that a predefined continuity risk requirement is met,

and evaluates the resulting impact on integrity risk. The paper does not present a landmark selection method, but is an incremental step towards extracting the set of features that maximizes safety performance.

To narrow down the scope of the paper, we must first define the continuity risk as it specifically applies to laser-based navigation, which has not been done before. In this paper, a set of features will be extracted only if it meets a predefined separation threshold. Thus, to mirror the aviation's definition of continuity threats that are *unscheduled* mission interruptions [19], this paper addresses loss of continuity due to *unexpectedly* low separation between extracted features. Lack of predictability is caused by sensor and map uncertainty. In other words, the continuity risk is the probability of not extracting a feature which was supposed to be extracted because of sensor error. Similar to GNSS, there will be other sources of loss of continuity [28, 29] that will be addressed in future work.

Following the above definition, areas of sparsely distributed landmarks can prevent laser-based navigation, but do not cause loss of continuity as long as they can be scheduled, e.g., using a map or using previous observations of landmarks. Insufficient landmarks are a source of availability risk, which can be mitigated using multi-sensor approaches that are beyond the scope of this work.

Thus, this paper assumes either a pre-established map, or prior observations of static landmark features. Many sophisticated algorithms have been devised to extract such features [1-15], and specific FE implementation detail are not discussed here. In practice, misleading-feature detection and exclusion methods must be used to deal with miss-extracted, non-static, and non-repeatedly-identified features that are not addressed in this work. Instead, the starting point of this paper is that the few most reliably recognizable features are repeatedly extracted, with a feature estimation error that can be linearly modeled and stochastically bounded using [30, 31]. The objective is to quantify the safety risks involved in FE and DA.

The second section of this paper introduces a probabilistic measure of the system's ability to distinguish landmarks, which is instrumental to prevent incorrect associations. The normalized separation between features is evaluated for all possible landmark permutations within a set. Features that can be exploited in this research not only include landmark position and orientation, but also size, surface color, reflectivity, roughness, or any other measurable characteristic. The minimum feature separation can be determined at FE using current sensor data (no association needed), and can be also be predicted using a landmark map or prior observations. We use this minimum separation metric to compare expected versus measured separation and to establish an upper-bound on the continuity risk. A minimum separation threshold is established to meet a predefined continuity requirement.

This threshold is used in the third section of this paper to refine the integrity risk bound derived in [15]. DA is performed using a nearest neighbor criterion [1], defined by the minimum normalized norm of the EKF innovation vectors over all possible landmark permutations. A multiple-hypotheses approach is employed to assess the impact on integrity risk of incorrect associations. An analytical integrity risk bound is obtained by incorporating the continuity-based minimum separation threshold defined above.

In the fourth section, the FE and DA integrity and continuity risk monitoring methods are evaluated by covariance analysis, for landmark geometries representing an APV passing by two point-features. The results illustrate the fact that the estimation error covariance is not an accurate measure of safety performance. In contrast, the integrity risk bound derived in this paper does account for potential incorrect associations.

Preliminary experimental testing is carried out in the fifth section. A set of data was collected in a structured environment using a multi-sensor system made of two two-dimensional laser scanners mounted back to back, and a carrier phase differential GPS implementation. This data is analyzed to assess the sensitivity of the integrity risk bound to varying values of the continuity risk requirement.

CONTINUITY RISK OF FEATURE EXTRACTION

This section first describes a normalized measure of separation between landmark features. The minimum separation can be computed at FE without requiring DA. It can be established in parallel using current sensor data and using a map of previously observed features, so that expected and measured separation can be compared. This comparison is the basis for continuity risk evaluation. In addition, the minimum separation within a set of features is determined by considering all possible permutations. This multiple-hypothesis approach will become useful again in the next section because the mean separation vectors and mean EKF innovation vectors are related.

Normalized Measure of Separation Between Features

Let n_L be the total number of visible landmarks, and m_F the number of feature parameters estimated per landmark. Depending on the sensor system, feature parameters can include a variety of measured characteristics such as position, orientation, size, and surface properties. The total number of feature parameters within the visible landmark set is: $n \equiv n_L m_F$. We can stack the actual (true) values of the extracted feature parameters for all landmarks in an $n \times 1$ vector $\mathbf{z}$. Let $\hat{\mathbf{z}}$ be an estimate of $\mathbf{z}$. Vector $\hat{\mathbf{z}}$, the extracted feature parameter measurement vector, is normally distributed with mean $\mathbf{z}$ and covariance matrix $\mathbf{V}$. We use the notation:

$$\hat{\mathbf{z}} \sim N(\ \mathbf{z}\ ,\ \mathbf{V}) \tag{1}$$

At the FE step, all feature measurements $\hat{\mathbf{z}}$ are known for an arbitrary ordering of the landmarks. If n_L landmarks are extracted, there are $(n_L!)$ potential landmark permutations, i.e., $(n_L!)$ ways to arrange the feature measurements in (1), which we will call $(n_L!)$ candidate associations in the next section of the paper. To determine the separation between all visible landmarks, we consider a comprehensive set of landmark permutations matrices noted $\mathbf{A}_i$, for $i = 1,..., h$, where the number of non-identity permutations is $h = n_L!-1$. We also define matrices $\mathbf{B}_i$ as $\mathbf{B}_i \equiv \mathbf{I}_n - \mathbf{A}_i$, for $i = 1,..., h$, where $\mathbf{I}_a$ is the $a \times a$ identity matrix.

As an illustrative example, consider the case where permutation '$i = 1$' is used to evaluate the separation between landmark '1' and landmark '2'. $\mathbf{A}_i$ and $\mathbf{B}_i$ take the following forms:

$$\mathbf{A}_1 = \begin{bmatrix} \mathbf{0}_{m_F \times m_F} & \mathbf{I}_{m_F} & \mathbf{0}_{m_F \times (n-2m_F)} \\ \mathbf{I}_{m_F} & \mathbf{0}_{m_F \times m_F} & \mathbf{0}_{m_F \times (n-2m_F)} \\ \mathbf{0}_{(n-2m_F) \times m_F} & \mathbf{0}_{(n-2m_F) \times m_F} & \mathbf{I}_{n-2m_F} \end{bmatrix}, \quad \mathbf{B}_1 = \begin{bmatrix} \mathbf{I}_{m_F} & -\mathbf{I}_{m_F} & \mathbf{0}_{m_F \times (n-2m_F)} \\ -\mathbf{I}_{m_F} & \mathbf{I}_{m_F} & \mathbf{0}_{m_F \times (n-2m_F)} \\ \mathbf{0}_{(n-2m_F) \times m_F} & \mathbf{0}_{(n-2m_F) \times m_F} & \mathbf{0}_{(n-2m_F) \times (n-2m_F)} \end{bmatrix} \tag{2}$$

where $\mathbf{0}_{a \times b}$ is an $a \times b$ matrix of zeros. For a permutation i, the following estimated landmark 'separation' vector is defined:

$$\hat{\mathbf{d}}_i \equiv \mathbf{B}_i \hat{\mathbf{z}} \tag{3}$$

$$\hat{\mathbf{d}}_i \sim N(\ \mathbf{d}_i\ ,\ \mathbf{D}_i\ ) \quad \text{where} \quad \mathbf{D}_i \equiv \mathbf{B}_i \mathbf{V} \mathbf{B}_i^T \tag{4}$$

and where $\mathbf{d}_i$ is the true value (or mean value) of the separation vector while $\hat{\mathbf{d}}_i$ is its estimated value. $\mathbf{B}_i$ is rank deficient, with rank values ranging from m_F to $n - m_F$ depending on how many landmarks are involved in permutation i, for $i = 1,..., h$. Let r_i be the rank of $\mathbf{B}_i$. An orthogonal decomposition of the symmetric positive semi definite matrix $\mathbf{D}_i$ is expressed as:

$$\mathbf{D}_i = \begin{bmatrix} \mathbf{U}_i & \mathbf{U}_{i,0} \end{bmatrix} \begin{bmatrix} \mathbf{S}_i & \mathbf{0}_{r_i \times (n-r_i)} \\ \mathbf{0}_{(n-r_i) \times r_i} & \mathbf{0}_{(n-r_i) \times (n-r_i)} \end{bmatrix} \begin{bmatrix} \mathbf{U}_i^T \\ \mathbf{U}_{i,0}^T \end{bmatrix} = \mathbf{U}_i \mathbf{S}_i \mathbf{U}_i^T \tag{5}$$

where $\mathbf{S}_i$ is a $r_i \times r_i$ diagonal matrix of non-zero singular values, and $\mathbf{U}_i$ is a $n \times r_i$ matrix such that $\mathbf{U}_i^T \mathbf{U}_i = \mathbf{I}_{r_i}$. For each permutation, we can define the $r_i \times 1$ normalized separation vector $\hat{\boldsymbol{\eta}}_i$ as:

$$\hat{\boldsymbol{\eta}}_i \equiv \mathbf{S}_i^{-1/2} \mathbf{U}_i^T \hat{\mathbf{d}}_i \tag{6}$$

$$\hat{\boldsymbol{\eta}}_i \sim N(\boldsymbol{\eta}_i \ , \ \mathbf{I}_{r_i}) \quad \text{where} \quad \boldsymbol{\eta}_i \equiv \mathbf{S}_i^{-1/2}\mathbf{U}_i^T\mathbf{d}_i \ . \tag{7}$$

Let $\hat{d}_i^2$ be the measured separation metric, which we choose to be the norm squared of $\hat{\boldsymbol{\eta}}_i$:

$$\hat{d}_i^2 \equiv \hat{\boldsymbol{\eta}}_i^T\hat{\boldsymbol{\eta}}_i = \hat{\mathbf{d}}_i^T\mathbf{U}_i\mathbf{S}_i^{-1}\mathbf{U}_i^T\hat{\mathbf{d}}_i \tag{8}$$

Using the norm operator, $\hat{d}_i$ can be expressed as: $\hat{d}_i = \left\|\hat{\boldsymbol{\eta}}_i\right\|$. $\hat{d}_i^2$ is non-centrally chi-square distributed with r_i degrees of freedom and with non-centrality parameter noted d_i^2 . We use the notation:

$$\hat{d}_i^2 \sim \chi^2(r_i \ , \ d_i^2) \quad \text{where} \quad d_i^2 \equiv \left\|\boldsymbol{\eta}_i\right\|^2 = \mathbf{d}_i^T\mathbf{U}_i\mathbf{S}_i^{-1}\mathbf{U}_i^T\mathbf{d}_i \tag{9}$$

Let $\bar{\mathbf{z}}_i$ be the expected feature parameter value, obtained either from a map ($\bar{\mathbf{z}}_i = \overline{\mathbf{m}}_i$) or from previous observations of landmark feature parameters ($\bar{\mathbf{z}}_i = \mathbf{h}_i(\bar{\mathbf{x}})$). We assume that $\bar{\mathbf{z}}_i \sim N(\mathbf{z}_i \ , \ \overline{\mathbf{V}}_i)$. At FE, current-time measured landmark features have not been associated with expected ones (no DA yet), so that landmark orderings in $\hat{\mathbf{z}}$ and $\bar{\mathbf{z}}_i$ do not necessarily match. Substituting $\bar{\mathbf{z}}_i$ and $\overline{\mathbf{V}}_i$ for $\hat{\mathbf{z}}$ and $\mathbf{V}$ in equations (1) to (9), the 'expected' (instead of 'measured') feature separations $\bar{d}_j$, for $j = 1,..., h$ can be computed. The notations $\hat{d}_i$ (hat-symbol) and $\bar{d}_j$ (bar-symbol) are used to distinguish measured versus expected quantities, which are impacted by different sensor/map errors. Different indices (i versus j) are used because the ordering of landmark subset separations does not match in general.

In order to compare the two sets of separation metrics, we use the minimum measured separation $\hat{d}$ and the minimum expected separation $\bar{d}$ defined as:

$$\hat{d} \equiv \min_{i=1,..,h}(\hat{d}_i) \quad \text{and} \quad \bar{d} \equiv \min_{j=1,..,h}(\bar{d}_j) \ . \tag{10}$$

We assume that the same set of landmarks is observed and expected. The case where this assumption is not satisfied can be addressed by FE algorithm design and by misleading-feature detection/exclusion, which will be tackled in future work.

Bounding the Continuity Risk of Feature Extraction

Let C_{REQ} be a predefined continuity risk requirement, as specified for example aviation applications in [19]. To ensure that C_{REQ} is achieved, a continuity criterion is defined, expressing that a set of landmarks is extracted if and only if:

$$\hat{d} \geq T \tag{11}$$

where T is the FE threshold. T is set to ensure that the continuity risk, or probability of loss of continuity (LOC), is smaller than C_{REQ} . The following equation can be used to determine T :

$$P_{LOC} \equiv P(\hat{d} < T \mid \bar{d}) \leq C_{REQ} \tag{12}$$

The distribution of $\hat{d}^2$ given in (9) is unknown because the non-centrality parameter d^2 is unknown. But, we can use $\bar{d}$ as a noisy estimate of d .

Appendix A describes a two-step process to determine T while taking into account uncertainty in $\hat{d}$ and $\bar{d}$. The continuity risk requirement is allocated between these two steps following the equation:

$$C_{REQ} = \hat{C}_{REQ} + \overline{C}_{REQ} \tag{13}$$

The first step provides a probabilistic lower-bound L_D on d, which ensures that the following inequality is satisfied:

$$P(d < L_D \mid \bar{d}) \le \overline{C}_{REQ}. \tag{14}$$

The resulting value of L_D is then employed to upper-bound P_{LOC}, starting from the definition in (12), and using the law of total probability and (14) in the following inequalities:

$$\begin{aligned} P_{LOC} &= P(\hat{d} < T \cap d \ge L_D \mid \bar{d}) + P(\hat{d} < T \cap d < L_D \mid \bar{d}) \\ &\le P(\hat{d} < T \cap d \ge L_D) + P(d < L_D \mid \bar{d}) \\ &\le P(\hat{d} < T \mid d \ge L_D) + \overline{C}_{REQ} \end{aligned} \tag{15}$$

where we used the bound $P(d \ge L_D) \le 1$, and we assumed that $\bar{d}$ and $\hat{d}$ were independent random variables. Thus, to ensure $P_{LOC} \le C_{REQ}$, the following inequality must be satisfied: $P(\hat{d} < T \mid d \ge L_D) \le \hat{C}_{REQ}$.
The second step of the derivation in Appendix A shows that:

$$P(\hat{d} < T \mid d \ge L_D) \le P(\hat{\varepsilon}_D > L_D - T) \tag{16}$$

where the distribution of $\hat{\varepsilon}_D^2$ is known: $\hat{\varepsilon}_D^2$ is centrally chi-square distributed with a number of degrees of freedom r_D such that $m_F \le r_D \le n - m_F$. It is conservative with respect to P_{LOC} to assume $r_D = m_F$: $\hat{\varepsilon}_D^2 \sim \chi^2(m_F, 0)$.
Finally, the continuity threshold T is obtained using the following equation:

$$P\left(\hat{\varepsilon}_D^2 > (L_D - T)^2\right) = \int_{(L_D - T)^2}^{+\infty} \chi_\alpha^2(m_F, 0)\, d\alpha = \hat{C}_{REQ} \tag{17}$$

The above two step FE threshold determination process is illustrated in Fig. 2.

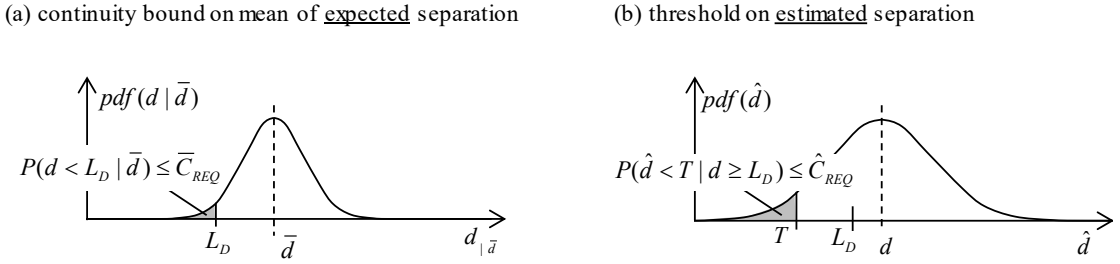

Fig. 1 Schematic Representation of the Two-Step Threshold Determination Process to Ensure a Predefined Continuity Risk Requirement

INTEGRITY RISK EVALUATION FOR FEATURE EXTRACTION AND DATA ASSOCIATION

Our approach to bound the integrity risk, or probability of hazardous misleading information $P(HMI)$, leverages the FE step to ensure that features are distinguishable, hence easier to associate. The objective is to guarantee, with quantifiable integrity, that there is a minimum distance between landmarks.

In this section, an integrity bound on the actual separation between estimated landmark features d_i, for all permutations $i = 1,..., h$, is established using the separation threshold T defined in (20). This bound is then used in the innovation-based multiple-hypothesis integrity risk evaluation method derived in [15]. We obtain an analytical upper-bound on $P(HMI)$ accounting for the probability of incorrect association (IA) and constrained to a continuity risk requirement.

Integrity Lower-Bound on True Feature Separation

Using the same notations as in the previous section, if n_L landmarks are extracted, there are $(n_L!)$ potential candidate associations between extracted features and mapped landmarks. Subscript i designates association hypotheses, for $i = 0,...,h$, where $h = n_L! - 1$. We define $i = 0$ the correct association (CA) hypothesis, the other h hypotheses are IA. The FE criterion specifies that no landmark is extracted if $\hat{d}_i < T$ so that data association (DA) can only be performed under the condition $\hat{d}_i \geq T$.

The innovation-based method derived in [15] to evaluate $P(HMI)$ assumes a lower-bound L_i on the mean separation d_i to bound the norm of the EKF innovations for association candidates $i = 0,...,h$. The following derivation establishes with quantifiable confidence the value of L_i, for $i = 1,..., h$. The larger L_i is, the lower the $P(HMI)$-bound becomes [15]. Therefore, we want to find the largest L_i that satisfies the following inequality:

$$P(d_i \leq L_i \mid \hat{d}_i \geq T) \leq I_{FE,REQ,i} \tag{18}$$

where $I_{FE,REQ,i}$ is a sub-allocation of $I_{FE,REQ}$, which is itself a small fraction of the overall integrity risk requirement I_{REQ}. $I_{FE,REQ}$ is divided among the h IA hypotheses as:

$$\sum_{i=1}^{h} I_{FE,REQ,i} = I_{FE,REQ} \quad \text{e.g.,} \quad I_{FE,REQ,i} = I_{FE,REQ}/h \tag{19}$$

Using steps similar to the derivation in Steps 1 and 2 of the Appendix, the left-hand-side in (18) can be bounded using the following inequalities:

$$\begin{aligned} P(d_i \leq L_i \mid \hat{d}_i \geq T) &\leq P(d_i - \hat{d}_i \leq L_i - \hat{d}_i \mid \hat{d}_i \geq T) \\ &\leq P(d_i - \hat{d}_i \leq L_i - T) \\ &\leq P(\hat{d}_i - d_i \geq T - L_i) \\ &\leq P\left(\left\|\hat{\boldsymbol{\eta}}_i\right\| - \left\|\boldsymbol{\eta}_i\right\| \geq T - L_i\right) \\ &\leq P\left(\left\|\hat{\boldsymbol{\eta}}_i - \boldsymbol{\eta}_i\right\| \geq T - L_i\right) \\ &\leq P(\hat{\varepsilon}_{D,i} \geq T - L_i) \end{aligned} \tag{20}$$

where

$$\hat{\varepsilon}_{D,i} \equiv \left\|\hat{\boldsymbol{\eta}}_i - \boldsymbol{\eta}_i\right\| \quad , \quad \hat{\varepsilon}_{D,i}^2 \sim \chi^2(r_i, 0) \tag{21}$$

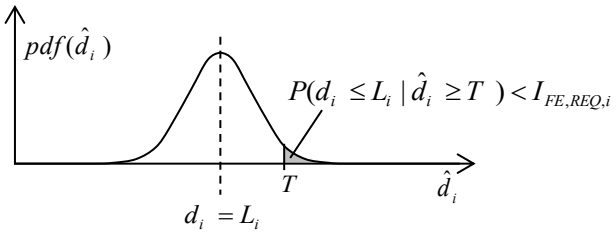

Fig. 2 Schematic Representation of the Process used to Determine a Lower-Bound 'L_i' on the Mean Separation 'd_i' that is Guaranteed with a Predefined Integrity Risk Allocation $I_{FE,REQ,i}$

Fig. 2 provides an illustration of the variables in (20): we want to find the largest mean value $d_i = L_i$ such that the probability of $\hat{d}_i$ exceeding T is lower than $I_{FE,REQ,i}$. Substituting (20) into (18), the integrity bound L_i can be determined using the following equation:

$$P\left(\hat{\varepsilon}_{D,i}^2 \ \ge \ (T - L_i)^2 \ \right) = \int_{(T-L_i)^2}^{+\infty} \chi_\alpha^2(r_i \ , \ 0) \ d\alpha = I_{FE,REQ,i} \quad , \quad \text{for } i = 1,..., \ h \tag{22}$$

L_i is the minimum value of the mean separation vector norm squared d_i that can be ensured with probability larger than $1 - I_{FE,REQ,i}$. If $L_i \ge T$, the integrity allocation cannot be met. If $L_i < T$, we have ensured with pre-allocated integrity that:

$$d_i^2 \ge L_i^2 \tag{23}$$

Innovation-Based Multiple-Hypothesis Integrity Risk Evaluation

Reference [15] describes a method to evaluate the integrity risk in the presence of potential incorrect associations. It uses a nearest neighbor association criterion [1] defined by the minimum norm of EKF innovation vectors weighted by the inverse innovation covariance matrix $\mathbf{Y}_i^{-1}$, over all possible landmark permutations $i = 0,..., \ h$. Let y_i be the mean value of the innovation norm. y_i is remarkable in that it is only zero for the correct association ($y_0 = 0$, $y_i \ne 0$ for $i \ne 0$), which makes it a pertinent indicator of IA. y_i is the true, sensor-error-free value of the innovation norm and is unknown.

Reference [15] shows that y_i can be lower-bounded using the following inequality:

$$y_i^2 \ge d_i^2 \lambda_{MIN,i}^2 \tag{24}$$

where $\lambda_{MIN,i}^2$ is the minimum eigenvalue of $(\mathbf{U}_i \mathbf{S}_i^{1/2} \mathbf{U}_i^T \mathbf{Y}_i^{-1} \mathbf{U}_i \mathbf{S}_i^{1/2} \mathbf{U}_i^T)$. But, d_i^2 is unknown. Fortunately, y_i^2 can be further lower-bounded using (23) so that we obtain:

$$y_i^2 \ge L_i^2 \lambda_{MIN,i}^2 \tag{25}$$

This result is used to establish an analytical bound on the integrity risk $P(HMI_k)$ at a time step k, which accounts for the risk of incorrect association. The integrity risk is expressed as [15]:

$$P(HMI_k) \le 1 - \left[1 - P(HMI_k \mid CA_K)\right] \prod_{q=1}^{k} P(CA_q \mid CA_{Q-1}) + I_{FE,REQ,k} \tag{26}$$

with

$$P(HMI_k \mid CA_K) = Q\left(\ell / \sigma_k\right) + 1 - Q\left(-\ell / \sigma_k\right) \tag{27}$$

$$P(CA_q \mid CA_{Q-1}) \geq 1 - P\left(r_q^2 \geq \min_{i=1,\ldots,h} \left\{ L_{i,q}^2 \lambda_{MIN,i,q}^2 / 4 \right\} \right) \tag{28}$$

where

k , q are indexes identifying time steps

K , Q we use the notation 'capital letter K ' to designate a range of indices: $K \equiv \{0,\ldots,k\}$

CA_K is the correct association hypothesis for all landmarks at all times

$Q(\ )$ is the tail probability function of the standard normal distribution

ℓ is the required alert limit that defines a hazardous situation, as specified in [19] for example aviation applications

σ_k is the standard deviation of the EKF pose estimation error for the vehicle state of interest (e.g., lateral deviation may be of primary concern for an APV staying in its lane)

$I_{FE,REQ,k}$ is a predefined integrity risk allocation at FE, chosen to be a small fraction of the overall integrity risk requirement $I_{REQ,k}$.

r_q^2 is a chi-square distributed random variable with a number of degrees of freedom that is the sum of the number of measurements and of EKF states at time step q

$L_{i,q}^2$ is defined at FE in (22), and represents the minimum value of the mean separation vector norm squared that is measured at FE at time step q .

$\lambda_{MIN,i,q}^2$ can be determined at DA, and is defined to account for the worst-case projection of the FE's separation vector into the DA's innovation space.

The analytical integrity risk bound in (26) to (28) not only accounts for the risk $P(HMI_k \mid CA_K)$ that can be directly derived from the EKF covariance matrix assuming correct association (CA), but it also accounts for the probability of correct association at all current and past time steps $\prod_{q=1}^{k} P(CA_q \mid CA_{Q-1})$. This bound is implemented, analyzed, and tested in the next two sections.

COVARIANCE ANALYSIS

In this section, an example simulation is employed to evaluate (26) to (28). The scenario is an illustrative two-dimensional, two-landmark problem. Covariance can be analyzed assuming flawless FE and DA. However, the integrity risk bound in (26) to (28) will show cases where the covariance does not capture aspects of safety risk due to incorrect associations (IA). Thus, this scenario helps quantify the impact of IA on $P(HMI_k)$, and shows the sensitivity of $P(HMI_k)$ to continuity risk requirement.

Illustrative 'Two Distinguishable Landmark' Scenario

Fig. 3 represents a vehicle designated by an upward pointing triangle roving between two landmarks represented by black-shaded circles. The vehicle starts at an initial, known position at point (0, 0) in a local East-North reference frame, and uses measurements from a laser or radar to estimate its position while moving northwards. In this example, vehicle orientation is known (as if given by another sensor, e.g., a perfect inertial navigation system). While roving along the North axis, the vehicle passes by two point-feature landmarks. The actual landmark locations are initially unknown to the navigation system. Landmark locations are simultaneously estimated with vehicle pose in a SLAM-type approach. Simulation parameters are listed in Table 1.

Positioning errors at consecutive sample updates are represented by covariance ellipses in Fig. 3, for the locations of the vehicle (red ellipses) and landmarks (blue ellipses). These ellipses assume consistently successful FE and DA. We focus on the East-West positioning error, perpendicular to vehicle's straight line trajectory. Cross-track errors are of primary concern for APV navigation safety, and the cross-track direction is where errors are the largest. A cross-track drift over distance travelled is observed, which is typical of SLAM [13, 32, 33].

Table 1: Simulation parameters

System Parameters	Values
Standard deviation on raw ranging measurement in (2)	0.02 m
Standard deviation on raw angular measurement in (2)	0.5 deg
Laser range Limit	20 m
Laser data sampling interval	0.5 s
Vehicle speed	1 m/s
Alert limit ℓ	0.5 m
Integrity risk allocation for FE, $I_{FE,REQ,k}$	10^{-8}
Continuity risk allocation for FE, $C_{FE,REQ,k}$	10^{-2} to 10^{-6}

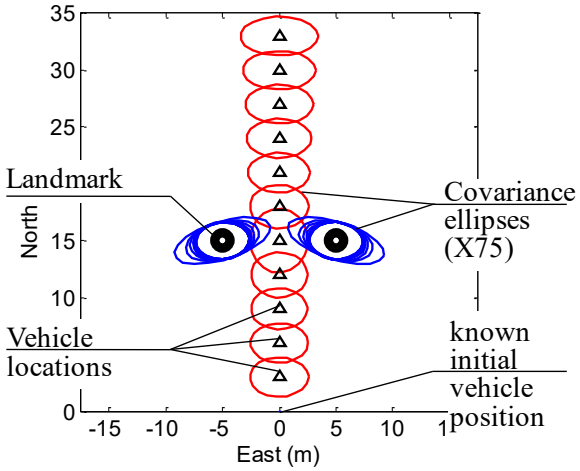

Fig. 3 Covariance Analysis for the Illustrative 'Two Distinguishable Landmark' Scenario

In this first 'distinguishable landmark scenario', the actual landmark locations are at (-5, 15) and (5, 15). This relatively large separation makes them easy to distinguish. It is worth noticing for the upcoming comparison with the next scenario that the blue covariance ellipses for the left and right landmarks do not overlap; this can give an indication of separation magnitude.

Fig. 4 shows the integrity risk bound labeled $P(HMI_k)$, represented with a solid red curve for $C_{REQ,k}=10^{-6}$, versus northward travel distance as the vehicles passes by the two landmarks. The bound is always larger than $I_{FE,REQ,k}=10^{-8}$, which corresponds to our choice of an example integrity risk requirement allocation $I_{FE,REQ,k}=10^{-8}$. As captured in (26), this $P(HMI_k)$-bound is loose when $P(CA_K)\approx 1$ and $P(HMI_k \mid CA_K) << 10^{-8}$, which is the case in Fig. 4 for travel distances smaller than 30 m. The $P(HMI_k)$-bound captures the risk involved in FE, and is a practical bound when trying to achieve an overall example requirement of $I_{REQ,k}=10^{-7}$.

In parallel, the black curve in Fig. 4 represents the bound on $P(HMI_k \mid CA_K)$, which is fully determined by the alert limit ℓ and the vehicle positioning covariance. This curve represents a vehicle navigation performance metric often used to evaluate laser-based navigation systems [13, 32, 33]. The black curve converges with our integrity risk bound (red curve) for travel distances larger than 30 m. In this example, the black curve adequately captures the safety risk, because $P(CA_K)\approx 1$. The next subsection shows that it is not always the case. Finally, Fig. 4 indicates that, in presence of widely separated landmarks, $P(HMI_k)$ is not sensitive to the continuity risk requirement since the curves for $C_{REQ,k}=10^{-2}$ and $C_{REQ,k}=10^{-6}$ overlap.

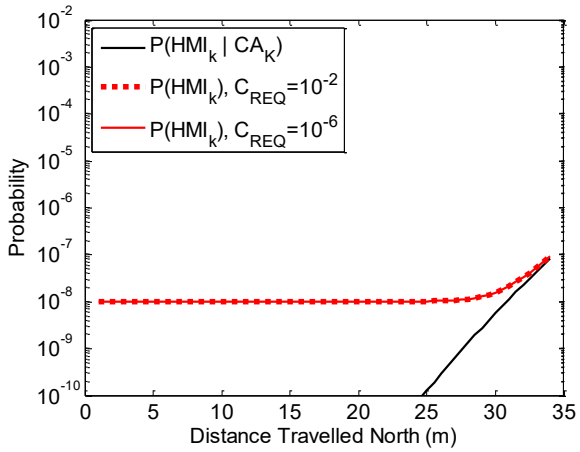

Fig. 4 Integrity Risk Bound for the Illustrative 'Two Distinguishable Landmark' Scenario. The red integrity risk ($P(HMI_k)$) curves do not reach lower than 10^{-8} because of our choice of $I_{FE,REQ,k}=10^{-8}$

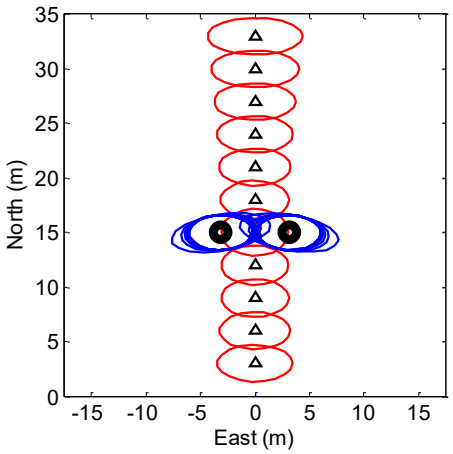

Fig. 5 Covariance Analysis for the Illustrative Two Difficult-to-Distinguish Landmark Scenario

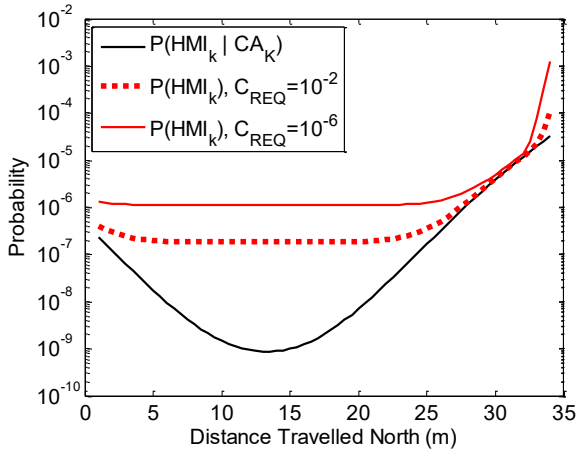

Fig. 6 Integrity Risk Bound for the Illustrative Two Difficult-to-Distinguish Landmark Scenario

Illustrative 'Two Difficult-to-Distinguish Landmark' Scenario

In this second case, the two landmark locations represented in Fig. 5 are at (-3, 15) and (3, 15). This makes them difficult to distinguish as suggested by the blue covariance ellipses that overlap from one landmark to the other.

Fig. 6 displays the $P(HMI_k)$-bounds in red, and the $P(HMI_k \mid CA_K)$-bound in black, versus travel distance. All curves are orders of magnitude higher than in Fig. 4. This is because the change in geometry between vehicle and landmarks provides less information on vehicle cross-track deviation in Fig. 5 than it did in Fig. 3. (The estimation process is detailed in [34].) This can also be seen with the red ellipses, which are horizontally more elongated in Fig. 5 as compared to Fig. 3.

The $P(HMI_k)$-bound shows the impact of possible incorrect associations on the integrity risk. It can be noted that there is a substantial difference between the red and black curves, especially for a travel distance of 15 m where the vehicle is right between landmarks. In this case, the covariance-based $P(HMI_k \mid CA_K)$-bound is orders of magnitude below the $P(HMI_k)$-bound. From a safety perspective, the covariance is a misleading navigation performance metric.

In addition, Fig. 6 shows that, in the presence of poorly separated landmarks, $P(HMI_k)$ can be very sensitive to the continuity risk requirement: there is almost an order of magnitude difference between the thick dotted red curve for $C_{REQ,k} = 10^{-2}$ and the thinner solid red curve for $C_{REQ,k} = 10^{-6}$. The method that we used to quantify the impact of $C_{REQ,k}$ on $P(HMI_k)$ using analytical results is a key contribution of this paper.

PRELIMINARY EXPERIMENTAL TESTING

Preliminary experimental testing of our proposed method is carried out using data collected in a structured environment shown in Fig. 7. Static simple-shaped landmarks are located at locations sparse enough to ensure successful outcomes for FE and DA. Because the results presented here are free of incorrect associations, they describe the estimation process, and $P(HMI_k)$ is expected to match $P(HMI_k \mid CA_K)$. Also, because landmarks are widely separated, the sensitivity of $P(HMI_k)$ to $C_{REQ,k}$ is expected to be small, similar to the case displayed in Fig. 4.

Measurements from carrier phase differential GPS (CPDGPS) as well as laser scanners are synchronized and recorded. In order to obtain a full 360 deg laser scan, two 180deg laser scanners are assembled back-to-back. The laser scanners have a specified 15-80 m range limit, a 0.5 deg angular resolution, a 5 Hz update rate and a ranging accuracy of 1-5 cm (1 sigma) [35]. The GPS antenna is mounted on top of the front laser. The lever-arm distance between the two lasers is included in the measurement model.

The two lasers and the GPS antenna are mounted on a rover also carrying the GPS receiver and data-link. An embedded computer onboard the vehicle records all measurements including the raw GPS data from the reference station transmitted via wireless spread-spectrum data-link. Truth vehicle trajectory and landmark locations are obtained using a fixed CPDGPS solution.

In this 'forest-type scenario', landmarks are tree-trunks reproduced using five cardboard columns and one dark plastic garbage can. Because there is actually no physical obstruction to the sky, satellite masking for the GPS/laser integration system is performed artificially as illustrated in Fig. 7: an artificially simulated tree canopy blocks high-elevation satellite signals; low-elevation GPS observations are not used either inside the obstruction.

As mentioned in the first paragraph of this section, the landmark geometry in this experiment is such that the risk of incorrect association is extremely small. This is confirmed on the upper chart in Fig. 8 where the actual error (thick line) fits the covariance envelope (thin line) throughout the test. The lower graph also shows that the $P(HMI_k)$-bound matches the $P(HMI_k \mid CA_K)$-bound, except between 565 m and 600 m of travel distance where the predefined integrity risk allocation for FE ($I_{FE,REQ,k} = 10^{-8}$) is the dominant term in the $P(HMI_k)$-bound. Also, because landmarks are clearly distinguishable, the $P(HMI_k)$-bound is expectedly insensitive to the continuity risk requirement $C_{REQ,k}$, which is consistent with the result in Fig. 4.

This test demonstrates that the method derived in this paper can be implemented using actual data from a multi-sensor GPS/laser system, and that the analytical integrity risk bound is tight when the risk of incorrect association is small. Further experimental validation in more realistic environments will be carried out in future work.

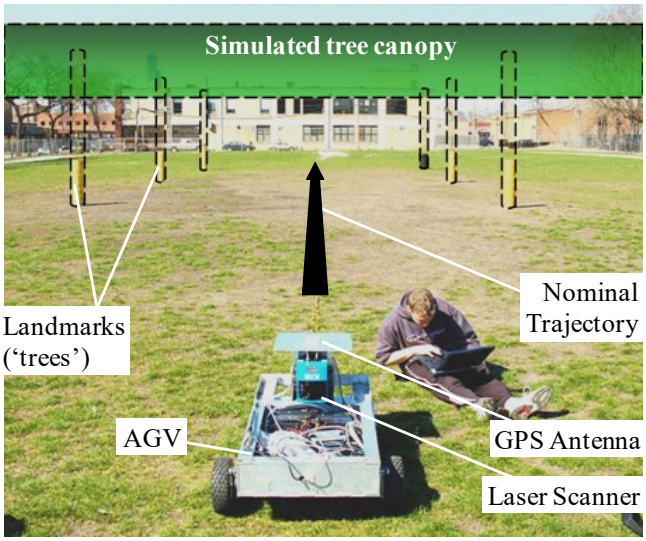

Fig. 7 Experimental Setup of a Forest-Type Scenario, where a GPS/Laser-Equipped Rover is driving by Six Landmarks (Cardboard Columns) in a GPS-Denied Area. GPS is Artificially Blocked by a Simulated Tree Canopy, and a Precise Differential GPS Solution is used as Truth Trajectory.

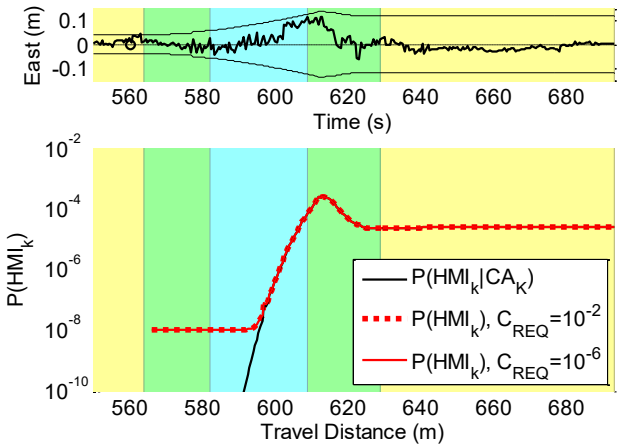

Fig. 8 (*TOP*) Cross-Track Positioning Error (thick black line) and Covariance Envelope (thin line), and (*BOTTOM*) Integrity Risk Bounds Versus Travel Distance for the Preliminary Experimental Data Set Capturing a Forest-Type Scenario. The vehicle started in a GPS-available area (yellow-shaded) and entered a transitional GPS-and-laser-available area (green) where absolute landmark position start being estimated; the vehicle then travels through a GPS obstruction and relies on laser/radar-only (blue-shaded area), so that the vehicle pose estimation error increases with travel distance; the vehicle finally gets back into a GPS available area (yellow), and the cross-track positioning drift is stopped.

CONCLUSION

This paper presents a new approach to ensure the safety of laser or radar-based navigation using feature extraction (FE) and data association (DA) by quantifying the integrity risk, while guaranteeing a required level of continuity.

Analytical integrity and continuity risk bounds are established, which account for failures in FE and DA. This paper focuses on establishing a minimum normalized separation metric ensuring, in a statistically quantifiable manner, that landmarks are distinguishable. An FE-criterion is designed to achieve a pre-defined continuity risk requirement. Then, this FE criterion is exploited at DA, where an innovation-based nearest-neighbor association criterion is employed to evaluate the risk of all potential incorrect associations, at each time step in the iterative vehicle pose estimation process.

Performance evaluations are carried out by covariance analysis, showing that the positioning error covariance is an incomplete and misleading safety performance metric, and quantifying the impact on integrity risk of the continuity risk requirement: the integrity risk is most sensitive when landmarks are poorly separated. In this case, the more stringent the continuity risk requirement is, the higher the integrity risk becomes. This is a key tradeoff in navigation safety, and is demonstrated here for the first time in laser-based localization using FE and DA.

Finally, preliminary experimental testing was carried out using a multi-sensor GPS/laser system onboard a vehicle roving in a structured environment. It showed that the integrity risk evaluation method can be implemented with real data. Future testing will be performed in a more realistic passenger vehicle operating environment.

APPENDIX

This appendix aims at (*Step 1*) establishing a LOC probability bound L_D on the true minimum separation between landmarks d, and (*Step 2*) deriving an upper bound on $P(\hat{d} < T \mid d \geq L_D)$ so that the FE continuity threshold T can be determined.

Step 1: Probability bound on the true separation

The first step of the derivation aims at finding L_D, such that $L_D < \bar{d}$, to satisfy (14): $P(d < L_D \mid \bar{d}) \leq \bar{C}_{REQ}$. $\bar{C}_{REQ}$ and $\bar{d}$ are given, L_D and d are unknown, but $\bar{d}$ provides a noisy measure of d. The following inequalities are used:

$$\begin{aligned} P(d < L_D \mid \bar{d}) &\leq P(d - \bar{d} < L_D - \bar{d} \mid \bar{d}) \\ &\leq P(\bar{d} - d > \bar{d} - L_D \mid \bar{d}) \\ &\leq P\left(\left\|\bar{\boldsymbol{\eta}}\right\| - \left\|\boldsymbol{\eta}\right\| > \bar{d} - L_D \mid \bar{d}\right) \\ &\leq P\left(\left\|\bar{\boldsymbol{\eta}} - \boldsymbol{\eta}\right\| > \bar{d} - L_D \mid \bar{d}\right) \\ &\leq P\left(\bar{\varepsilon}_D > \bar{d} - L_D \mid \bar{d}\right) \end{aligned}$$

where $\bar{\boldsymbol{\eta}}$ is the normalized expected separation vector and $\bar{\varepsilon}_D^2$ is the expected separation error squared ($\bar{\varepsilon}_D^2 \equiv \left\|\bar{\boldsymbol{\eta}} - \boldsymbol{\eta}\right\|^2$). $\bar{\boldsymbol{\eta}}$ corresponds to the minimum expected separation, i.e., $\bar{\boldsymbol{\eta}}$ is $\bar{\boldsymbol{\eta}}_j$ for j defined using (10) as: $\arg\min_{j=1,\ldots,h}(\bar{d}_j)$. The $r_j \times 1$ vectors $\bar{\boldsymbol{\eta}}_j$ where r_j is the rank of $\mathbf{B}_j$, for $j = 1,\ldots, h$, are derived using the same equations as (3) to (7), except that subscripts i are replaced with j, $\hat{\mathbf{z}}$ in (3) is replaced with $\bar{\mathbf{z}}_i$, and $\mathbf{V}$ in (4) is replaced with $\bar{\mathbf{V}}$. The above derivation uses the reverse triangle inequality:

$$\bar{d} - d = \left\|\bar{\boldsymbol{\eta}}\right\| - \left\|\boldsymbol{\eta}\right\| \leq \left| \left\|\bar{\boldsymbol{\eta}}\right\| - \left\|\boldsymbol{\eta}\right\| \right| \leq \left\|\bar{\boldsymbol{\eta}} - \boldsymbol{\eta}\right\|$$

In addition, $\bar{\varepsilon}_D^2$ is centrally chi-square distributed with a number of degrees of freedom r: $m_F \le r \le n - m_F$, and it is conservative with respect to continuity risk to assume $\bar{\varepsilon}_D^2 \sim \chi^2(m_F\ ,\ 0)$. The lower bound L_D is determined using the equation:

$$P\left(\bar{\varepsilon}_D^2 > (\bar{d} - L_D)^2 \right) = \int_{(\bar{d}-L_D)^2}^{+\infty} \chi_\alpha^2(m_F\ ,\ 0)\ d\alpha = \overline{C}_{REQ}$$

Step 2: Upper bound on $P(\hat{d} < T \mid\ d \ge L_D)$

The second part of this Appendix aims at showing that: $P(\hat{d}\ < T \mid\ d \ge L_D) \le P(\ \hat{\varepsilon}_D > L_D - T)$. We will use this inequality to find the FE threshold T such that $T < L_D$, to guarantee that $P_{LOC} \le C_{REQ}$. We consider the following inequalities:

$$\begin{aligned} P(\hat{d}\ < T \mid\ d \ge L_D) &\le P(\hat{d} - d\ < T - d \mid\ d \ge L_D) \\ &\le P(\hat{d} - d\ < T - L_D) \end{aligned}$$

The threshold T will be selected such that $T < L_D$. In addition, by definition in (12), the event $\hat{d} - d \ge 0$ is not a continuity issue because, when this event occurs, $\hat{d} \ge d \ge L_D > T$ (in accordance with the conditional event on the left-hand side of the above inequalities, and with the definition of P_{LOC} in (12)). Thus, the only LOC case to consider is $\hat{d} - d < 0$, so that both sides of the inequality in the above bound are negative. $P(\hat{d}\ < T \mid\ d \ge L_D)$ can be further bounded using the following inequalities:

$$\begin{aligned} P(\hat{d}\ < T \mid\ d \ge L_D) &\le P(\ |\hat{d} - d| > L_D - T) \\ &\le P(\ \left\|\hat{\boldsymbol{\eta}} - \boldsymbol{\eta}\right\| < L_D - T) \\ &\le P(\ \hat{\varepsilon}_D > L_D - T) \end{aligned}$$

where $\hat{\boldsymbol{\eta}}$ is the normalized estimated separation vector and $\hat{\varepsilon}_D^2$ is the estimated separation error squared ($\hat{\varepsilon}_D^2 \equiv \left\|\hat{\boldsymbol{\eta}} - \boldsymbol{\eta}\right\|^2$). $\hat{\boldsymbol{\eta}}$ corresponds to the minimum estimated separation, i.e., $\hat{\boldsymbol{\eta}}$ is $\hat{\boldsymbol{\eta}}_i$ for i defined using (10) as: $\arg\min_{i=1,..h}(\hat{d}_i)$. The above derivation uses the reverse triangle inequality:

$$|\hat{d} - d| = \left|\ \left\|\hat{\boldsymbol{\eta}}\right\| - \left\|\boldsymbol{\eta}\right\|\ \right| \le \left\|\hat{\boldsymbol{\eta}} - \boldsymbol{\eta}\right\| = \hat{\varepsilon}_D$$

and proves that $P(\hat{d}\ < T \mid\ d \ge L_D) \le P(\ \hat{\varepsilon}_D > L_D - T)$.

REFERENCES

[1] Y. Bar-Shalom, and T. E. Fortmann, "Tracking and Data Association," Mathematics in Science and Engineering, Vol. 179, Academic Press, 1988.

[2] T. Bailey, "Mobile Robot Localisation and Mapping in Extensive Outdoor Environments," PhD Dissertation, The University of Sydney, 2002.

[3] T. Bailey and J. Nieto, "Scan-SLAM: Recursive Mapping and Localisation with Arbitrary-Shaped Landmarks," Workshop at IEEE RSS 2008, Zurich, Switzerland, 2008.

[4] A.J. Cooper, "A Comparison of Data Association Techniques for Simultaneous Localization and Mapping," M.S. Thesis, Massachussetts Institute of Technology, 2005.

[5] S. T. Pfister, K. L. Kriechbaum, S. I. Roumeliotis, J. W. Burdick, "Weighted Range Sensor Matching Algorithms for Mobile Robot Displacement Estimation," Proc IEEE ICRA, 2002.
[6] S.T. Pfister, S.I. Roumeliotis, J.W. Burdick, "Weighted Line Fitting Algorithms for Mobile Robot Map Building and Efficient Data Representation Robotics and Automation," Proc. IEEE ICRA, 2003.
[7] I. Tena Ruiz, Y. Petillot, D. M. Lane, and C. Salson, "Feature Extraction and Data Association for AUV Concurrent Mapping and Localisation," Proc. IEEE-ICRA, 2001.
[8] S. Thrun, "Robotic Mapping: A Survey," Exploring Artificial Intelligence in the New Millenium, G. Lakemeyer and B. Nebel, February 2002.
[9] S. Thrun, W. Burgard, and D. Fox, "A Real-Time Algorithm forMobile Robot MappingWith Applications to Multi-Robot and 3D Mapping," Proc. IEEE ICRA 2000, San Francisco, CA, 2000.
[10] V. Nguyen, A. Martinelli, N. Tomatis, and R. Siegwart, "A Comparison of Line Extraction Algorithms using 2D Laser Rangefinder for Indoor Mobile Robotics," Proc. IEEE/RSJ IROS, 2005.
[11] Nunez, P.; Vazquez-Martin, R. del Toro, J.C. Bandera, A., "Feature Extraction from Laser Scan Data based on Curvature Estimation for Mobile Robotics," Proc. IEEE ICRA, 2006.
[12] Y. Li, E.B. Olson, "A general purpose feature extractor for light detection and ranging data," Sensors, Vol. 10, No. 11, 2010.
[13] R. Madhavan, H. Durrant-Whyte, and G. Dissanayake, "Natural Landmark-based Autonomous Navigation using Curvature Scale Space," Proc. IEEE-ICRA, 2002.
[14] D. Maksarov, and H. Durrant-Whyte, "Mobile Vehicle Navigation in Unknown environments: a multiple hypothesis approach," Proc. IEEE Control Theory Applications, Vol. 142 No. 4, 1995, pp. 385-400.
[15] M. Joerger, M. Jamoom, M. Spenko, and B. Pervan, "Integrity of Laser-Based Feature Extraction and Data Association," Proceedings of IEEE/ION PLANS 2016, Savannah, GA, April 2016, pp. 557-571.
[16] E. Ackerman, "Google's Autonomous Cars Are Smarter Than Ever at 700,000 Miles," 2014.
[17] fars.NHTSA.dot.gov. Fatality analysis reporting system. Technical report, National Highway Traffic and Safety Administration, 2014.
[18] National Highway Traffic Safety Administration. National motor vehicle crash causation survey: Report to congress. Technical Report DOT HS 811 059, U.S. Department of Transportation, 2008.
[19] RTCA Special Committee 159, "Minimum Aviation System Performance Standards for the Local Area Augmentation System (LAAS)," RTCA/DO-245, 2004, Appendix D.
[20] Y.C. Lee, "Analysis of Range and Position Comparison Methods as a Means to Provide GPS Integrity in the User Receiver," Proc. of the 42nd Annual Meeting of The Institute of Navigation, Seattle, WA, 1986, pp. 1-4.
[21] B.W. Parkinson, and P. Axelrad, "Autonomous GPS Integrity Monitoring Using the Pseudorange Residual," NAVIGATION, Vol. 35, No. 2, 1988, pp. 225-274.
[22] RTCA Special Committee 159, "Minimum Operational Performance Standards for Global Positioning System/Wide Area Augmentation System Airborne Equipment," RTCA/DO-229C, 2001, pp. 1-21.
[23] J. Leonard, and H. Durrant-Whyte, "Directed Sonar Sensing for Mobile Robot Navigation," Kluwer Academic Publishers, Cambridge, MA, 1992, pp. 129-138.
[24] S.B. Williams, G. Dissanayake, and H. Durrant-Whyte, "An efficient Approach to the Simultaneous Localisation and Mapping Problem," Proc. IEEE-ICRA, 2002.
[25] M. Joerger, and B. Pervan, "Measurement-Level Integration of Carrier-Phase GPS and Laser-Scanner for Outdoor Ground Vehicle Navigation," ASME Journal of Dynamic Systems, Measurement, and Control, Vol. 131, 2009.
[26] Y. Bar-Shalom, F. Daum, and J. Huang, "The Probabilistic Data Association Filter," IEEE Control Systems Magazine, 2009, pp. 82-100.
[27] J. Areta, Y. Bar-Shalom, and R. Rothrock, "Misassociation Probability in M2TA and T2TA," J. of Advances in Information Fusion, Vol. 2, No. 2, 2007, pp. 113-127.
[28] M. Joerger, and B. Pervan, "Fault Detection and Exclusion Using Solution Separation and Chi-Squared RAIM," IEEE TAES, Vol. 52, No. 2, 2016.
[29] Y. Zhai, M. Joerger, and B. Pervan, "Continuity and Availability in Dual-Frequency Multi-Constellation ARAIM," *Proceedings of ION GNSS+ 2015*, Tampa, Florida, September 2015, pp. 664-674
[30] B. DeCleene, "Defining Pseudorange Integrity – Overbounding," Proc. of ION GPS 2000, Salt Lake City, UT., 2000, pp. 1916-1924.
[31] J. Rife, S. Pullen, P. Enge, and Boris Pervan, "Paired Overbounding for Nonideal LAAS and WAAS Error Distributions." IEEE TAES, Vol. 42, No. 4, 2006 pp. 1386-1395.
[32] F. Bayoud, "Vision-Aided Inertial Navigation Using a Geomatics Approach," Proc. ION GNSS, Long Beach, CA, 2005.
[33] G. Dissanayake, P. Newman, S. Clark, H. Durrant-Whyte, and M. Csorba. "A Solution to the Simultaneous Localization and Map Building (SLAM) Problem." IEEE Transactions on Robotics Automation. 17.3 (2001): 229-241

[34] M. Joerger, “Carrier Phase GPS Augmentation Using Laser Scanners and Using Low Earth Orbiting Satellites,” Ph.D. Dissertation, Illinois Institute of Technology,
[35] C. Ye, and J. Borenstein, “Characterization of a 2-D Laser Scanner for Mobile Robot Obstacle Negotiation,” Proc. IEEE-ICRA, May 2002.